

Article

The Influence of Lobe Top Clearance on the Performance of High-Speed Centrifugal Pumps

Dongxu Wang¹, Kai Wang², Ziqiang Wang¹, Dongwei Wu³ and Ying Song^{1,*}

¹ School of Water Conservancy and Architectural Engineering, Northwest A&F University, Yangling 712100, China; wangdongxu@nwafu.edu.cn (D.W.); 2023055847@nwafu.edu.cn (Z.W.)

² Academy of Aerospace Propulsion Technology, Xi'an 710100, China; wangkai_6y@163.com

³ Jiangsu Surveying and Design Institute of Water Resources Co., Ltd., Yangzhou 225127, China; 15240240208@163.com

* Correspondence: ysong0321@nwafu.edu.cn

Abstract: High-speed centrifugal pumps are widely used in several industries due to their high efficiency and small footprint. In actual applications, there are issues such as low operational efficiency and a small high-efficiency flow interval; particularly, the leakage occurring in the impeller channel gap presents a significant barrier to the pump's performance and stability. This study takes the fully open impeller miniature high-speed centrifugal pump as the object and uses a numerical simulation calculation method. The objective of this research endeavor is to analyze the effects of different flow conditions on a high-speed centrifugal pump's external characteristics, flow field characteristics, and energy loss. The findings indicate that lobe top clearance exerts a substantial impact on the efficiency of high-speed centrifugal pumps. Increasing the lobe top clearance will result in a reduction in pump head and efficiency, particularly under high flow conditions. The lobe top clearance has a significant impact on the complexity of the flow in the impeller, particularly the flow close to the suction surface of the impeller, according to an analysis of the flow field characteristics. The energy loss analysis further confirms the importance of reducing lobe top clearance for improving pump performance and reducing energy loss. These results provide valuable guidance for optimizing centrifugal pump designs with lobe top clearance.

Keywords: high-speed centrifugal pump; lobe top clearance; entropy production; numerical analysis



Citation: Wang, D.; Wang, K.; Wang, Z.; Wu, D.; Song, Y. The Influence of Lobe Top Clearance on the Performance of High-Speed Centrifugal Pumps. *Water* **2024**, *16*, 1943. <https://doi.org/10.3390/w16141943>

Academic Editors: Giuseppe Pezzinga and Wencheng Guo

Received: 3 June 2024

Revised: 5 July 2024

Accepted: 8 July 2024

Published: 10 July 2024



Copyright: © 2024 by the authors. Licensee MDPI, Basel, Switzerland. This article is an open access article distributed under the terms and conditions of the Creative Commons Attribution (CC BY) license (<https://creativecommons.org/licenses/by/4.0/>).

1. Introduction

The high-speed centrifugal pump, also known as the high-speed partial flow pump, is an innovative type of centrifugal pump. In both industrial facilities and everyday life, high-speed centrifugal pumps are likely to be among the most frequently employed kinds of apparatus. High-speed centrifugal pumps exhibit superior efficacy when contrasted with other types of rotating pumps [1–3]. They utilize the speed-increasing effect of a speed-increasing gearbox to significantly increase the rotational speed of the impeller, far exceeding that of a conventional centrifugal pump [4]. This results in a substantial increase in the fluid velocity along the outer edge of the impeller, thereby achieving a high lift effect. This kind of pump not only eliminates many disadvantages of the multistage pump, it also possesses the benefits of superior effectiveness, compact structure, and light weight. High-speed centrifugal pumps have found extensive application in industries such as petroleum refining, petrochemical, energy, chemical, food, and other applications since their inception, especially for small-flow and high-head purposes [5]. Through their unique working principle and excellent performance, high-speed centrifugal pumps have become indispensable and important equipment in modern industrial production.

However, open impeller centrifugal pumps encounter numerous challenges in practical applications [6]. These mostly consist of the leaking vortex issue resulting from the gap between the impeller blade tip and the housing. This leakage vortex leads to the

creation of an intricate flow pattern within the impeller, resulting in increased hydraulic losses and decreased pump head and efficiency. Furthermore, the unstable nature of the leakage vortex may generate low-frequency, high-amplitude pressure pulsations that can intensify pump vibrations and pose a threat to stability and safety [7]. Importantly, under off-design conditions, particularly at low flow rates, backflow at the inlet becomes more severe, further contributing to performance degradation. Additionally, flow separation and rotational stall phenomena are exacerbated at low specific speeds and non-design operating conditions, ultimately impacting pump efficiency and stability [8].

Currently, the research on high-speed centrifugal pumps is mainly concentrated on performance improvement and internal flow field analysis. In the field of selection optimization design and performance improvement, Cong Xiaoqing et al. [9] used CFX 2022 R2 software and the single factor sensitivity analysis method to conduct multi-objective optimization design of the primary structural parameters of high-speed centrifugal pumps. The optimization objectives involved the head, efficiency, and turbulent kinetic energy. Through the response surface optimization method, the optimal design parameters were obtained, significantly improving the pump's head and efficiency, reducing the maximum turbulent kinetic energy, and thus enhancing the hydraulic and fluid efficiency of the pump while minimizing energy usage. Zhou Zhihua et al. [10] found that minimizing the distance between the impeller and the throat ring can greatly enhance the pump's performance in terms of head and efficiency but leads to increased frictional losses. However, the benefits of reducing leakage losses are more significant overall, leading to an improvement in efficiency. Wang Rui [11] used an orthogonal experimental method to enhance the cavitation performance of a high-speed centrifugal pump by optimizing the geometric characteristics of the inducer wheel. Further optimization of the inducer wheel blade thickness, blade angle, and impeller inlet diameter was conducted to improve the overall efficiency of the pump. Ultimately, a comprehensive flow channel model was employed to computationally replicate the optimized high-speed centrifugal pump, examining the internal flow pattern and cavitation characteristics. Zhu Qiang [12] conducted hydraulic design pertaining to centrifugal pumps operating at high speeds and performed three-dimensional steady and unsteady computational fluid dynamics simulations for the designed high-speed centrifugal pumps to explore the pump's internal and external features, including the velocity and pressure distribution features, and examined the impact of the inducer wheel on the energy properties of the pump. Sha Yujun [13] studied centrifugal pumps' internal flow characteristics and explored the effects of balance holes on pump performance, the sealing effect of biomimetic honeycomb-shaped sealing rings, and the impact of pressure pulsations on the safety of the pump casing. He also found that by making initial modifications to the pump casing, the size of the pump casing could be diminished to a certain degree, while maintaining the efficiency of the pump. Zhao Lianming [14] used numerical simulation to examine the low specific speed high-speed centrifugal pumps' internal flow characteristics, the jet-vortex structure at the impeller output, the hump phenomenon in the $H-Q$ characteristic curve, and the pressure pulsation issue. The impeller was optimized using a staggered blade technology by changing the cutting position, azimuthal angle, and deflection angle of the blades to improve the pump's internal and external characteristics, reduce pressure pulsation, and increase the pump's efficiency and stability. Zhou Liming [15] used a combination of theoretical analysis and numerical simulation to optimize the hydraulic model of the centrifugal pump in an ultra-high-speed energy recovery unit based on the impact factor. Structural parameters such as the number of blades, outer diameter, inner diameter, blade shape, and tongue were optimized to boost the head and efficiency of the pump.

With the diversification of application scenarios and the complexity of operating conditions, higher requirements are presented for the efficient and steady performance of centrifugal high-speed pumps. Therefore, how to improve the unsteady internal flow of centrifugal high-speed pumps, increase the overflow rate, and reduce the hydraulic loss are the key issues to be addressed. Therefore, this paper takes a high-speed centrifugal pump with a fully open impeller as the research object and studies the influence law of

different conditions on the external characteristics, flow field characteristics, and energy loss of the high-speed centrifugal pump through numerical simulation, which provides certain theoretical references for an in-depth understanding of the complex flow in the pump and assurance of its safe and stable operation performance.

The complexity of the flow in the impeller, particularly the flow near the suction surface, is significantly influenced by the lobe top clearance, as determined by the analysis of flow field characteristics. The significance of minimizing lobe top clearance to enhance pump performance and minimize energy loss is further supported by energy loss analysis. The miniature high-speed centrifugal pump is exceptionally well-suited for the restricted space and resource conditions of the space station due to its compact size, low weight, and low power consumption. The deep examination of the lobe top clearance flow field characteristics of the micro high speed centrifugal pump not only reveals the internal flow mechanism of the pump, but also establishes a scientific foundation for the design optimization, performance enhancement, and fault prediction of the pump. This is of great importance in the technical advancement and industrial application of the pump equipment. Specific applications on the space station include the following: The water recovery system can utilize the miniature high-speed centrifugal pump to purify and repurpose astronauts' perspiration, breathing water, and effluent, as well as to guarantee that astronauts have a consistent supply of drinking water. Miniature high-speed centrifugal compressors can be employed in the environmental control system of the space station to propel the air flow, guarantee the uniform distribution and circulation of air, and maintain the appropriate temperature and humidity.

2. Computational Model

2.1. Geometric Model

The fundamental high-speed centrifugal pump design characteristics are: flow rate $0.96 \text{ m}^3/\text{h}$, head 26 m, speed 9400 r/min, specific speed 52. SOLIDWORKS 2022 R2 software is used to model the high-speed centrifugal pump, as shown in Figure 1. Table 1 displays the geometric specifications of the key parts of the high-speed centrifugal pump.

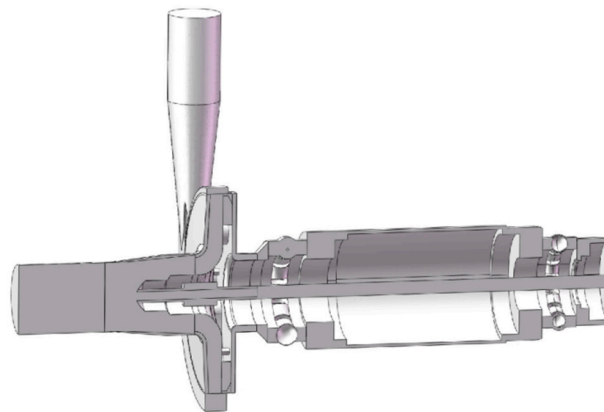


Figure 1. A 3D model of the high-speed centrifugal pump.

Table 1. Geometric parameters of the important components.

Parameter Name	Numerical Value
Impeller inlet diameter	16 mm
Impeller outlet diameter	45 mm
Impeller exit width	3 mm
Number of leaves of impeller	4 + 4
Base circle diameter of volute	46 mm
Volute inlet width	5 mm

The fluid domain of each centrifugal pump component is meshed using ICEM. Because of the high-speed centrifugal pump's intricate construction, in addition to the structural network divided by the lobe top clearance, unstructured mesh is used in other areas, and the complex flow area is encrypted to guarantee the precision of the computation outcomes, as shown in Figure 2.

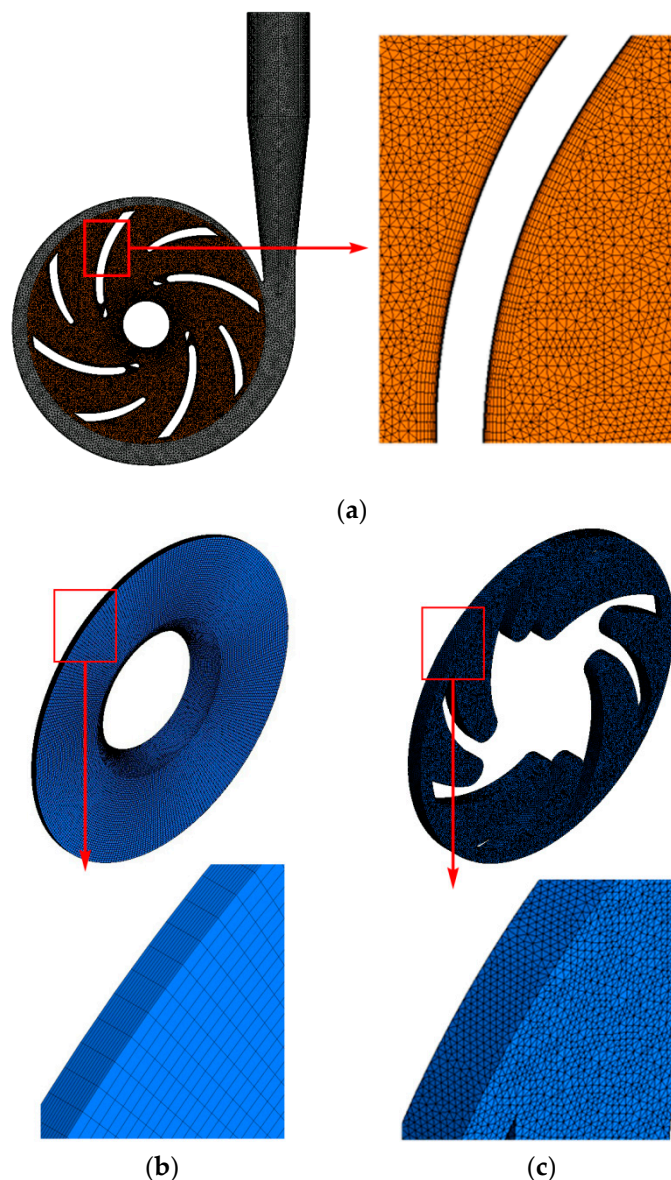


Figure 2. Fluid domain meshing: (a) volutes and impellers; (b) lobe top clearance; (c) rear cover plate.

The internal flow of a high-speed centrifugal pump is simulated using Ansys CFX 2022 R2 numerical software in this paper. Table 2 illustrates the boundary conditions.

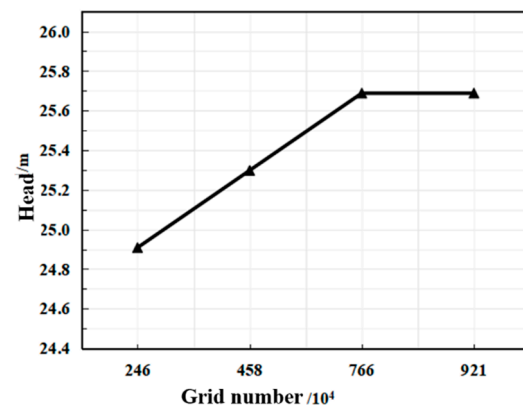
2.2. Grid Independence Verification

The number of grids is closely related to the calculation result and calculation time. Grid independence must be confirmed before solving in order to guarantee the accuracy of the solution results and remove the impact of the number of grids on the solution outcomes. Grid independence verification ensures that, once a given number of grids is reached, the computation results will stay the same and will not alter as the number of grids rises. Grid independence verification is an important prerequisite for accurate calculation results.

Table 2. Boundary conditions for numerical simulation.

Project	Condition
Software	Ansys CFX
Medium	Normal temperature and pressure water
Interface	Frozen Rotor
Turbulence model	Transient Rotor-Stator
Wall condition	RNG k- ϵ
Import conditions	No sliding wall
Outlet condition	Total pressure import
Reference pressure	Mass flow outlet
Unsteady calculation time step	0 Pa
Total time of unsteady calculation	1.7730×10^{-5} s (1° rotation time)
Convergence standard	2.5532×10^{-2} s (rotation time of 4 cycles)
	Residuals are less than 10^{-5}

In this paper, four sets of different numbers of grids are established, which are 2.46 million, 4.58 million, 7.66 million, and 9.21 million. The head is used as the reference standard for the steady computation, which is performed under the design flow condition. Figure 3 displays the grid independence verification findings. The graphic shows that when the number of grids grows, so does the computed head. When the number of grids reaches 7.66 million, the calculated head remains unchanged, and the error between the calculated head and the theoretical head is about 1.2%, which is within the acceptable range. At the same time, considering the impact of grid quantity on computation duration, this paper adopts the scheme of 7.66 million grids for subsequent calculation.

**Figure 3.** Grid independence verification.

2.3. Test Verification

To confirm the accuracy and dependability of the numerical simulation results of the high-speed centrifugal pump, it is imperative to evaluate the external characteristics of the model pump, which are then corroborated by the numerical simulation data. The test is conducted on the open test platform, as illustrated in Figure 4. The JN338 torque sensor (Worldcom Technology Co., Ltd., Beijing, China) measures the pump torque, the BFG-SDN50 electromagnetic flowmeter (Zhenghai Industrial Automation Equipment Co., Ltd., Xi'an, China) measures the flow, and the EJA510A pressure sensor (Zhenghai Industrial Automation Equipment Co., Ltd., Xi'an, China) measures the pressure of the inlet and exhaust section when the pump is operating. The high-speed centrifugal pump's fully open impeller and the entire machine are depicted in Figure 5.

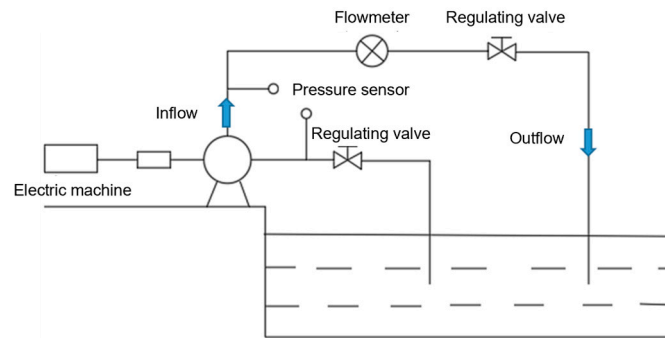


Figure 4. Experimental system of the high-speed centrifugal pump.



Figure 5. The whole high-speed centrifugal pump and the fully open impeller.

The external characteristics of the numerical simulation and the test are compared in Figure 6. The head and efficiency at each flow point are slightly lower than the simulated value as a result of the mechanical loss, mechanical seal, and other factors in the test process, as illustrated in the figure. However, the numerical simulation's evolving trends of the flow-head and flow-efficiency curves are consistent with the experimental results. The head error and efficiency error are less than 2% and 5%, respectively. The numerical analysis results of the high-speed centrifugal pump are particularly reliable when the RNG $k-\epsilon$ turbulence model and the grid number are 7.66×10^6 , as evidenced by the simulated and experimental errors of the head and efficiency of 1.04% and 1.93%, respectively, in the design condition.

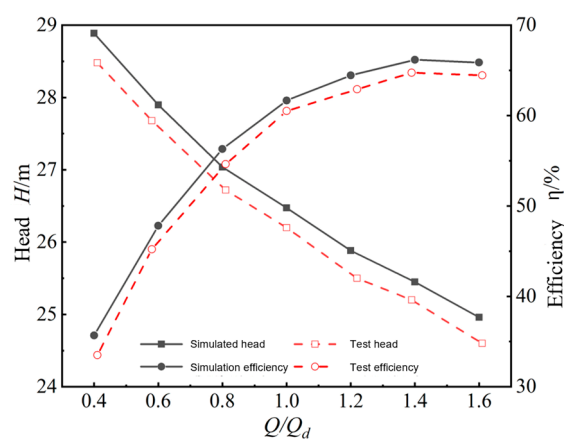


Figure 6. Comparison of external characteristics between numerical simulation and experimental results.

3. Numerical Calculation Theory

3.1. Control Equation

The principles of conservation of mass, energy, and momentum—the three laws of conservation of physics—impose restrictions on the flow of fluid. The basic governing equations of fluid mechanics describing fluid motion can be obtained by applying three

major physics conservation laws to a specific flow system: the energy conservation equation, momentum conservation equation (sometimes called the Navier–Stokes equation), and mass conservation equation (continuity equation), which constitute the theoretical basis of numerical simulation analysis and are widely used in CFD numerical analysis. Their specific expression is as follows:

(1) Mass conservation equation

In the context of flow problems, adherence to the law of conservation of mass is imperative. The principle states that the net mass entering a fluid cell during the same time interval is equivalent to the increase in mass per unit time within the cell. This principle enables the formulation of the mass conservation equation:

$$\frac{\partial \rho}{\partial t} + \frac{\partial(\rho u)}{\partial x} + \frac{\partial(\rho v)}{\partial y} + \frac{\partial(\rho w)}{\partial z} = 0 \quad (1)$$

In Formula (1), ρ represents density; t denotes time; and u , v , and w are the x , y , and z components of the velocity vector u , respectively.

(2) Momentum conservation equation

Additionally, every flow system must adhere to the first law of conservation of momentum. The law can be expressed as follows: the rate of change of the fluid's momentum in the microelement with regard to time is equal to the sum of the various external torques acting on the microelement. In fact, this is Newton's second law. Equations governing momentum conservation in the x , y , and z directions can be obtained using the following law:

$$\frac{\partial(\rho u)}{\partial t} + \text{div}(\rho u \mathbf{u}) = -\frac{\partial p}{\partial x} + \frac{\partial \tau_{xx}}{\partial x} + \frac{\partial \tau_{yx}}{\partial y} + \frac{\partial \tau_{zx}}{\partial z} + F_x \quad (2)$$

$$\frac{\partial(\rho v)}{\partial t} + \text{div}(\rho v \mathbf{u}) = -\frac{\partial p}{\partial y} + \frac{\partial \tau_{xy}}{\partial x} + \frac{\partial \tau_{yy}}{\partial y} + \frac{\partial \tau_{zy}}{\partial z} + F_y \quad (3)$$

$$\frac{\partial(\rho w)}{\partial t} + \text{div}(\rho w \mathbf{u}) = -\frac{\partial p}{\partial z} + \frac{\partial \tau_{xz}}{\partial x} + \frac{\partial \tau_{yz}}{\partial y} + \frac{\partial \tau_{zz}}{\partial z} + F_z \quad (4)$$

In the formula group (2)–(4), the vector symbol $\text{div}(\mathbf{a}) = \partial \mathbf{a}_x / \partial x + \partial \mathbf{a}_y / \partial y + \partial \mathbf{a}_z / \partial z$ is introduced, and p is the pressure on the fluid element; τ_{xx} , τ_{xy} , τ_{xz} is the component of the viscous stress τ on the surface of the microelement due to the molecular viscosity action. F_x , F_y , F_z is the physical force on the cell.

(3) Energy conservation equation

A fundamental principle, the law of conservation of energy, is applicable to heat exchange-based flow systems. The rate of energy increase in a cell is equivalent to the sum of the work performed by physical and surface forces on the cell and the net heat flux into the cell. In fact, this is the first law of thermodynamics.

$$\frac{\partial(\rho T)}{\partial t} + \text{div}(\rho u T) = \text{div}\left(\frac{k}{c_p} \mathbf{grad} T\right) + S_T \quad (5)$$

In Equation (5), c_p is the specific heat capacity; T is the temperature; k is the heat transfer coefficient of the fluid; S_T is the viscous dissipation term.

Note that although though the energy conservation equation serves as the fundamental formula for solving fluid flow and heat transfer problems, in the case of incompressible flows, the heat exchange may be too tiny to be taken into consideration; thus, the energy conservation equation is not considered. In this paper, the flow medium in the high-speed centrifugal pump is water, which is regarded as an incompressible fluid, the density remains unchanged, and the heat exchange amount is small. Simultaneous solutions are required for the momentum conservation equation and the mass conservation equation.

3.2. Entropy Production Theory

In this work, the medium for a high-speed centrifugal pump is water at normal temperature and pressure. It is generally considered that the work of fluid machinery is an adiabatic process; thus, the generation of entropy due to variations in temperature can be disregarded. According to the Reynolds mean simulation method, it is generally believed that the time mean velocity and pulsation velocity are the factors that contribute to the total entropy production rate of turbulent flow. In contrast to the turbulent dissipation entropy production rate (TEPR), which is caused by the pulsation velocity, the direct dissipation entropy production rate (DEPR) is the entropy production rate caused by the time-average velocity. The totality of the aforementioned rates constitutes the local entropy production rate (LEPR) of the complete system [16–21].

$$\dot{S}_D''' = \dot{S}_D''' + \dot{S}_{D'}''' \quad (6)$$

$$\dot{S}_D''' = 2\frac{\mu}{T} \left[\left(\frac{\partial \bar{u}}{\partial x} \right)^2 + \left(\frac{\partial \bar{v}}{\partial y} \right)^2 + \left(\frac{\partial \bar{w}}{\partial z} \right)^2 \right] + \frac{\mu}{T} \left[\left(\frac{\partial \bar{u}}{\partial y} + \frac{\partial \bar{v}}{\partial x} \right)^2 + \left(\frac{\partial \bar{u}}{\partial z} + \frac{\partial \bar{w}}{\partial x} \right)^2 + \left(\frac{\partial \bar{v}}{\partial y} + \frac{\partial \bar{w}}{\partial z} \right)^2 \right] \quad (7)$$

$$\dot{S}_{D'}''' = 2\frac{\mu}{T} \left[\left(\frac{\partial u'}{\partial x} \right)^2 + \left(\frac{\partial v'}{\partial y} \right)^2 + \left(\frac{\partial w'}{\partial z} \right)^2 \right] + \frac{\mu}{T} \left[\left(\frac{\partial u'}{\partial y} + \frac{\partial v'}{\partial x} \right)^2 + \left(\frac{\partial u'}{\partial z} + \frac{\partial w'}{\partial x} \right)^2 + \left(\frac{\partial v'}{\partial y} + \frac{\partial w'}{\partial z} \right)^2 \right] \quad (8)$$

where \dot{S}_D''' is the total entropy yield of turbulent flow; \dot{S}_D''' is the direct dissipation entropy production rate caused by time mean velocity; $\dot{S}_{D'}'''$ is the turbulent dissipation entropy production rate caused by pulsation velocity, $W/(m^3 \cdot K)$; $\bar{u}, \bar{v}, \bar{w}$ are the components of the time-mean velocity in the x, y, z directions; u', v', w' are the components of the pulsation velocity in the x, y, z directions, m^3/s ; μ is the dynamic viscosity, $N \cdot s/m^2$; T is the temperature, K.

The instantaneous mean velocity can be solved directly by using Reynolds mean method, but the pulsation velocity cannot be solved directly. Zhang Jianyi et al. [5] concluded through research that the turbulence model can be used to express the rate at which the pulsation velocity induces turbulence entropy production.

In model $k - \omega$, the equation for the tumultuous dissipation entropy production rate (9) can be defined as follows [21–25]:

$$\dot{S}_{D'}''' = \frac{\beta \rho \omega k}{T} \quad (9)$$

The turbulent dissipation entropy yield of the $k - \omega$ model adopted in this paper can be expressed by Equation (10) [26,27]:

$$\dot{S}_{D'}''' = \frac{\rho \varepsilon}{T} \quad (10)$$

where ρ is density, Kg/m^3 ; ε is the turbulent dissipation rate, m^2/s^3 ; T is the temperature, K.

Furthermore, due to the significant velocity gradient present in the wall region, entropy production has a strong wall effect; however, some previous studies did not take this into account, and thus the energy loss through entropy production was relatively small. Consequently, the entropy production rate caused by the wall, known as the wall entropy production rate (WEPR), needs to be included in the overall entropy production rate of the system. This may be computed using Equation (11) [28–31].

$$\dot{S}_W'' = \frac{\vec{\tau} \cdot \vec{v}}{T} \quad (11)$$

where $\vec{\tau}$ is wall shear stress, Pa; \vec{v} is the velocity vector in the wall region, m/s ; T is the temperature, K.

Three kinds of entropy yields can be obtained by integrating their respective calculation areas [32–37].

$$S_{pro,\bar{D}} = \int_V \dot{S}_{\bar{D}}''' dV \quad (12)$$

$$S_{pro,D'} = \int_V \dot{S}_{D'}''' dV \quad (13)$$

$$S_{pro,W} = \int_A \dot{S}_W'' dA \quad (14)$$

$$S_{pro} = S_{pro,\bar{D}} + S_{pro,D'} + S_{pro,W} \quad (15)$$

where $S_{pro,\bar{D}}$, $S_{pro,D'}$, $S_{pro,W}$, and S_{pro} represent total entropy production (TEP), direct entropy production (DEP), turbulent entropy production (TEP), and wall entropy production (WEP), respectively. Direct entropy production (DEP) and turbulent entropy production (TEP) together are called local entropy production or mainstream entropy production (LEP).

4. Results Analysis

4.1. Analysis of External Characteristics and Flow Field Characteristics

A total of seven different flow conditions were set up, and their steady calculation was carried out; the pump's external characteristics were examined in various flow conditions. The high-speed centrifugal pump's external characteristic curve is illustrated in Figure 7 under a variety of flow conditions. As the flow rate increases, the head of the high-speed centrifugal pump drops. The efficiency of the system improves as the flow rate increases, as long as the flow rate remains below 1.4 times the design flow rate (Q_d). However, if the flow rate surpasses 1.4 Q_d , the efficiency of the system drops somewhat. The point of maximum efficiency is at 1.4 times the quantity demanded (Q_d). The power loss of the fluid (such as friction loss and turbulence loss) increases as the flow rate in the runner of the impeller and pump increases. Furthermore, the efficacy and head of the pump may be diminished as a result of fluid flow separation within the impeller or pump housing, which can be induced by increased flow rates. The efficacy of the pump typically increases as the flow rate is increased from zero to 1.4 times the design flow rate. The reason for this is that the pump operates more closely to its design conditions in this range, energy conversion is more efficient, and hydrodynamic losses (primarily friction and turbulence losses) are relatively low. The efficacy begins to decrease when the flow rate exceeds 1.4 times the design flow rate. This is primarily due to the fact that high flow rates result in an increase in fluid power losses and can result in increased flow separation and backflow, which are significant sources of energy loss. Figure 8 illustrates the highest and lowest pressure levels as they change with the flow rate under different flow circumstances. Figure 8 demonstrates that the maximum pressure drops as the flow rate increases across different flow conditions. Nevertheless, the minimum pressure remains rather stable despite an increase in the flow rate.

Numerical simulations were conducted for three different heights of blade lobe top clearance in high-speed centrifugal pumps in seven distinct flow conditions, and CFD-Post software 2022 R1 was used to determine the performance and effectiveness of high-speed centrifugal pumps with varying blade lobe top clearances under varied flow circumstances. The results were then plotted on the external characteristic curves displayed in Figure 9. The top clearance of the high-speed centrifugal pump's head decreases with increasing flow rate, as seen by the external characteristic curve. This is because when the input power is unchanged, the total work done by the water body remains unchanged, without any change in the impeller speed. As the flow rate increases, the amount of water entering the pump increases during the same time, resulting in the work done by the unit water body decreasing and the head becoming smaller. Under the same flow conditions, the head decreases as the clearance of the lobe top increases, and the gap between the head of different lobe top clearance becomes larger and larger with the increase of flow rate. This may be due to the increase of lobe top clearance, the increase of clearance leakage flow,

the interaction between clearance flow and the main stream, the increase of pump content product loss, and the decrease of the impeller’s work on the water, resulting in the decrease of head.

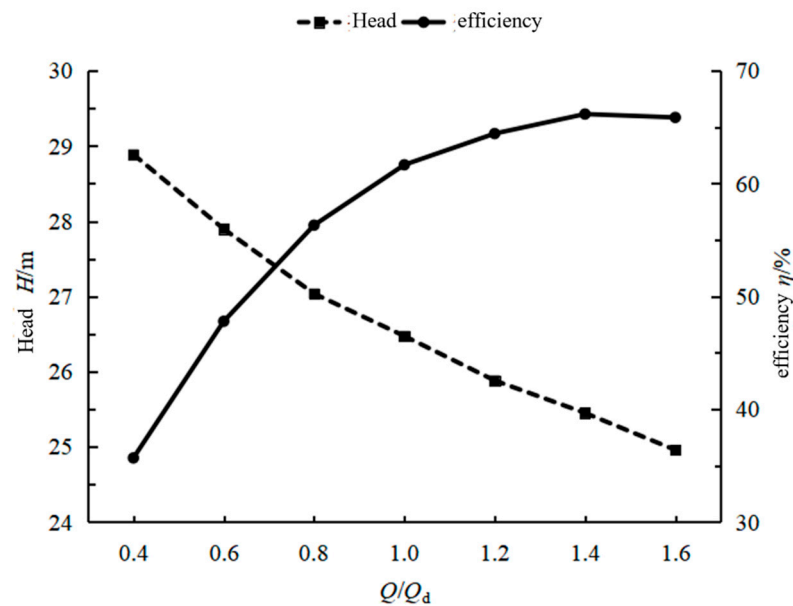


Figure 7. External characteristic curve of high-speed centrifugal pump under different flow conditions.

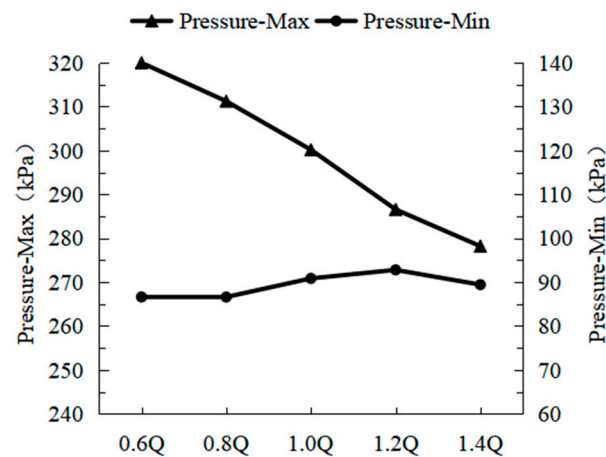


Figure 8. Under different flow conditions, the maximum and minimum values of pressure vary with the flow.

Figure 10 depicts the pressure distribution in the center region of the lobe top clearance layer of a high-speed centrifugal pump. The pump has three different lobe top clearances, and the measurements were taken under the prescribed flow circumstances. The figure illustrates that the pressure distribution pattern in the middle section of the lobe top clearance layer remains consistent under various tip gaps. It demonstrates a gradual increase in pressure from the inlet to the outlet along the flow direction, with the highest pressure occurring at the volute tongue. The pressure distribution exhibits a high degree of uniformity throughout the circumference, but the pressure contour at the upper part of the blade is curved to a certain extent, and the smaller the blade lobe top clearance, the more obvious the bending degree is. This is because a smaller clearance between the blade and the front cover will have a more obvious squeezing effect on the water flow, so the pressure contour will bend. The smaller the squeeze, the smoother the pressure contour. Figure 11 depicts the velocity pattern of the center part of the lobe top clearance layer under the specified flow condition. The overall distribution of speed is not significantly affected by

the change in lobe top clearance, as evidenced by the figure. The high speed zone is situated in the top section of the four primary blades, while the low speed zone is positioned in the upper part of the impeller runner. The interlingual region is where the most significant variation in speed takes place. However, the velocity distribution is different locally. With the increase of lobe top clearance, the low-speed zone of 0 m/s~1.5 m/s in the impeller runner tends to shrink. When the intrusion of the high-velocity zone near the lobe top clearance into the low-speed zone of the impeller runner is greater, it can be concluded that the increase of lobe top clearance aggravates the generation of clearance flow, resulting in enhanced backflow and increased energy loss at the lobe top clearance. As the reflux at the pharynx increases, the energy loss in the system will also increase. Friction losses, eddy current losses, and losses resulting from fluctuations in fluid acceleration comprise these energy losses. The backflow at the baffle tongue will generate unnecessary eddy currents, which will result in a reduction in system efficiency and an increase in friction and turbulence loss, particularly when the fluid passes through the impeller.

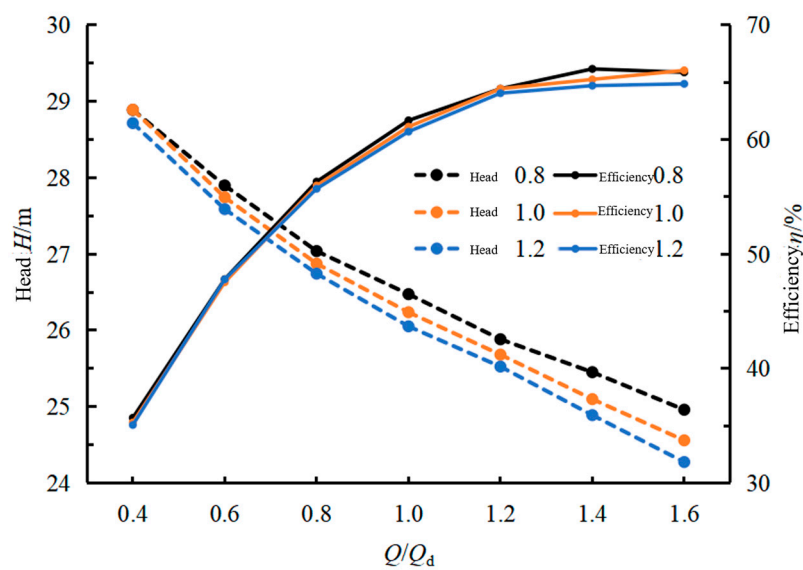


Figure 9. External characteristic curve of high-speed centrifugal pump with different lobe top clearance.

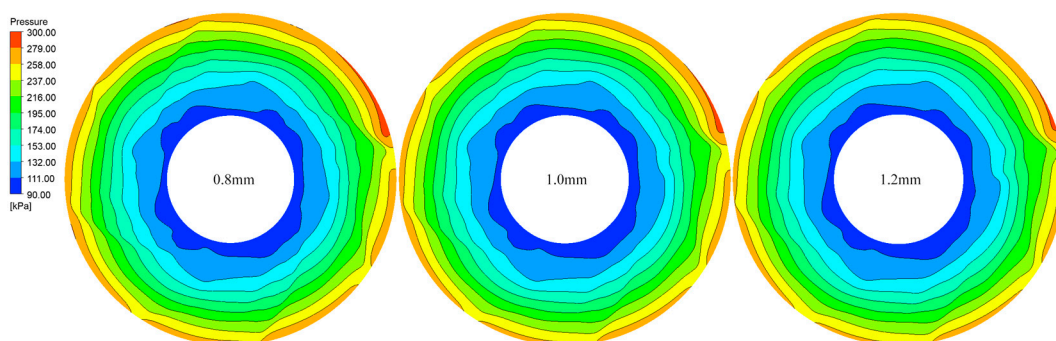


Figure 10. Pressure distribution in the middle section of lobe top clearance.

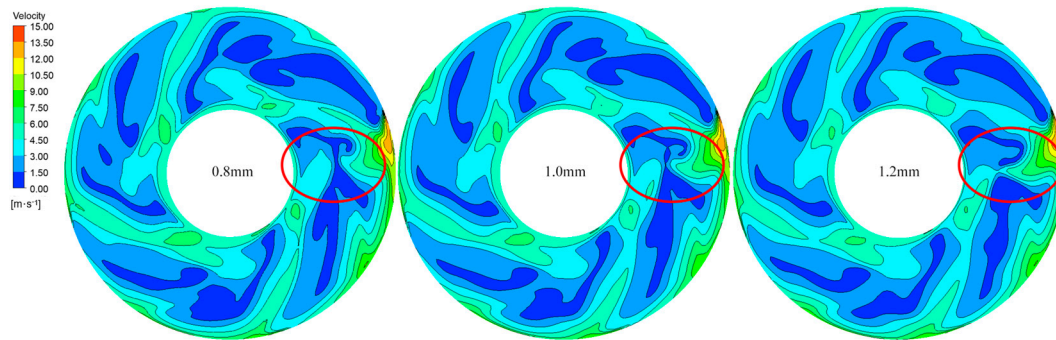


Figure 11. Velocity distribution in the middle section of lobe top clearance (Local differences are shown in red).

The velocity flow line distribution of various blade height sections in the impeller region is depicted in Figures 12–14, where the flow rate is designated. The impeller near the lobe top clearance is more significantly affected by the change in clearance value, as illustrated in the figure, but it has little effect on the far side. The 10% highest section of the blade of the impeller is far away from the lobe top clearance and is less affected by the clearance flow; therefore, the velocity distribution is nearly identical, and the flow line is uniform. This is due to the fact that these regions are more susceptible to interstitial flow, which leads to an increase in flow heterogeneity and turbulence. This, in turn, impacts the uniformity of the flow line and the quality of the flow state. Nevertheless, the flow is steadily stabilized in the region beyond the lobe top clearance, and the clearance flow’s influence is relatively negligible. Consequently, the velocity distribution is more consistent, the flow line is smoother, and the flow condition is satisfactory.

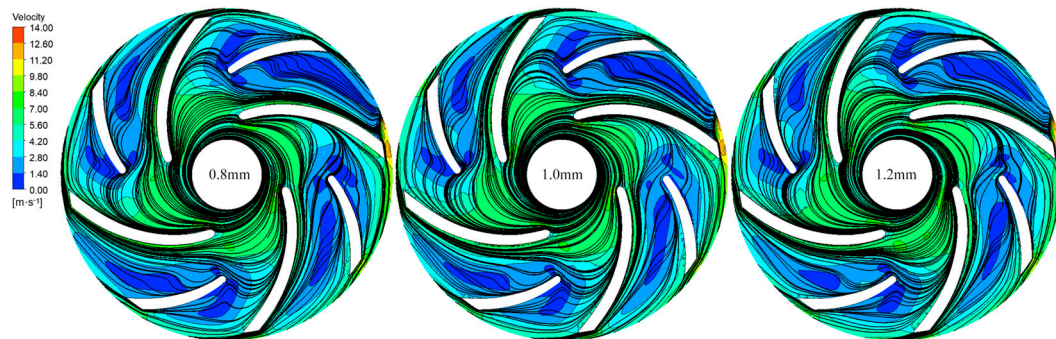


Figure 12. Velocity streamline distribution of 10% height section of blade of impeller.

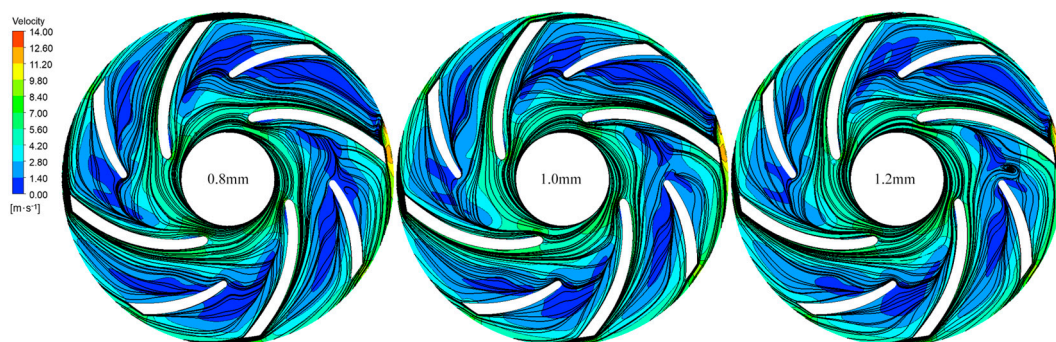


Figure 13. Velocity flow line distribution in the middle section of impeller.

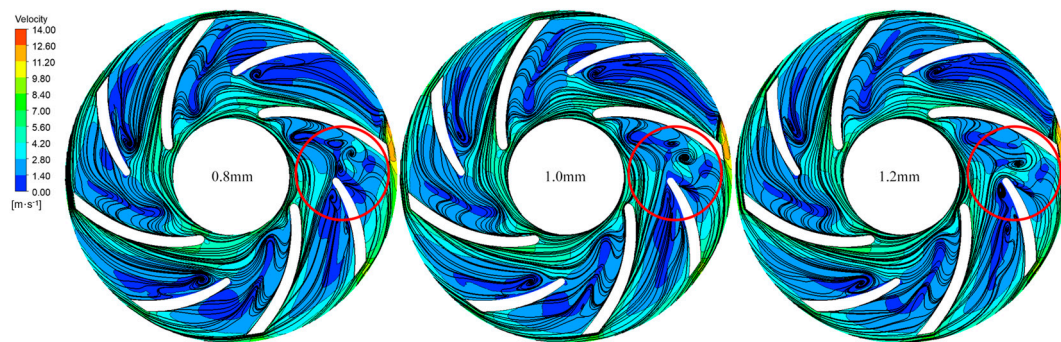


Figure 14. Velocity streamline distribution of 90% height section of blade of impeller (Local differences are shown in red).

The clearance flow is affected by the middle part of the impeller because it is close to the lobe top clearance. The flow line on the suction surface of the blade gradually narrows towards the inlet side of the blade, suggesting that the clearing flow moves from the blade tip to the suction surface side of the blade, enters the impeller flow channel, and combines with the main stream. A clearance value of 0.8 mm and 1.0 mm in the center part of the impeller does not result in the formation of a vortex in the flow channel close to the baffle tongue. Nevertheless, the clearance measurement of 1.2 mm leads to the occurrence of backflow and the dissipation of energy. This phenomenon occurs as a result of the intricate flow pattern at the baffle tongue and the reinforcement of the flow that occurs when there is a significant gap between components.

The 90% blade height section of the impeller is most affected by the lobe top clearance, and the flow line is most chaotic. A vortex forms at the suction surface of the short blade and becomes stronger and moves towards the departure side of the blade as the clearance value increases. There are numerous vortices in the vicinity of the baffle impeller's flow path (red circular position) at a clearance value of 0.8 mm, and these vortices develop into a large vortex when the clearance value increases to 1.0 mm; a new vortex emerges at the base of the little blade whenever the clearance value exceeds 1.2 mm. The findings of this investigation indicate that the impeller is notably influenced by the existence of lobe top clearance, which complicates the flow pattern and increases the hydraulic loss and energy dissipation as a consequence of the friction between the fluids.

4.2. Analysis of Energy Loss

The entropy production and proportion of each region are depicted in Figure 15 for a variety of gap values. The disparity increases, resulting in a 1–2% increase in the total entropy production depicted in the figure. The entropy production in the volute region is the highest for each clearance value, followed by that in the impeller and lobe top clearance regions. The energy loss in the high-speed centrifugal pump is not influenced by the change in clearance value, and it is primarily concentrated in the volute area, where it accounts for approximately 80% of the total. The clearance leakage intensity increases as the clearance value increases, which leads to a minor increase in the energy loss in the clearance region between the impeller and the tip. This is due to the fact that the change in clearance value will have a slight impact on the energy loss and entropy production within the centrifugal pump. This is primarily evident in the increase in leakage flow and the resulting slight increase in energy loss in the impeller and lobe top clearance region. Nevertheless, the volute region remains the most significant factor in determining the distribution of overall energy loss and the proportion of entropy production, as the resistance in the region is predominant.

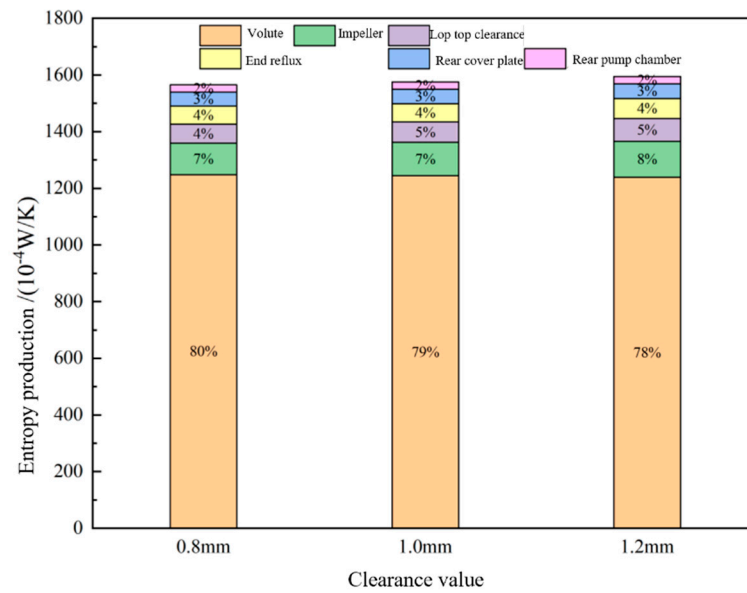


Figure 15. Entropy production and proportion of each region under different clearance values.

Figure 16 depicts the distribution of entropy generation across the main flow components of the high-speed centrifugal pump for different clearance levels. The local entropy production in the volute region is identical to that on the wall, as is evident from the figure. The alteration in gap value does not affect the distribution of the two forms of entropy production in the volute area. The primary source of entropy creation in the impeller and lobe top clearance zone is the local entropy production resulting from the velocity field. The local entropy production of the impeller and lobe top clearance region increases by 3% and 5%, respectively, from 0.8 mm to 1.2 mm, and the increase rate is not linear; the increase rate is larger from 0.8 mm to 1.0 mm, and the increase rate is relatively gentle from 1.0 mm to 1.2 mm. This shows that the increase of gap value is not uniform with the enhancement of gap leakage flow.

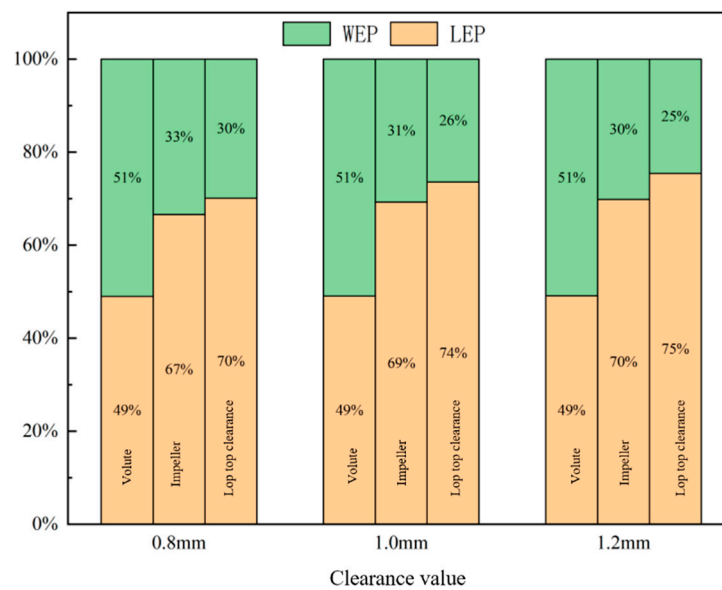


Figure 16. Entropy production of main flow parts of high-speed centrifugal pump under different clearance values.

Figure 17 illustrates the distribution of entropy production at the middle interface of the lobe top clearance for different degrees of clearance. The figure

illustrates that at various clearance values, regions of high entropy are concentrated near the tongue of the volute and above the blade. This suggests that the energy loss in these areas is greater, primarily due to the high flow velocity and large flow gradient. With the increase of the clearance value, the entropy yield begins to decrease, indicating that the increase of the clearance value can reduce the energy loss in the lobe top clearance region. Figure 15 demonstrates that when the clearance in the lobe top increases, there is a corresponding rise in energy loss. The reason for this is that the entropy yield indicates only the amount of energy lost per unit volume, whereas the integration of the entropy yield across the volume represents the overall energy loss. Nevertheless, the augmentation of the gap value will unavoidably result in the enlargement of the gap region's volume. This increase in volume assumes a prominent function in causing the overall energy loss to rise.

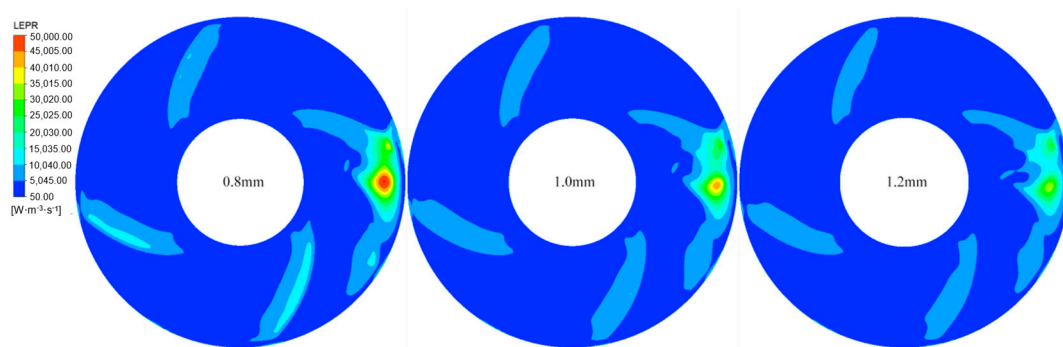


Figure 17. Distribution of local entropy production in the middle section of blade lobe top clearance under different gaps.

Figure 18 illustrates the distribution of the local entropy production rate in the vicinity of the tip section of the impeller region across a range of clearance values. As the clearance value increases, the region of high entropy yield near the blade suction surface and the interstitial tongue expands, as depicted in the figure. However, the maximum value of entropy yield decreases, and the area of high entropy yield near the interstitial tongue does not occupy the entire flow channel at 0.8 mm; it does at 1.2 mm. Figures 19 and 20 illustrate the distribution of local entropy production and wall entropy production in the volute region at varying clearance values. The flow of the volute is minimally affected by the change in lobe top clearance. This is due to the fact that the maximal entropy production rate decreases, but the region of high entropy production rate near the blade suction surface and septum tongue can expand as the clearance value increases. This phenomenon may be associated with the redistribution and reorganization of the flow structure. The change in clearance value may have a more substantial impact on the expansion rate of the high entropy yield region near the spacer tongue, whereas the flow in the volute region is minimally affected by the change in tip clearance.

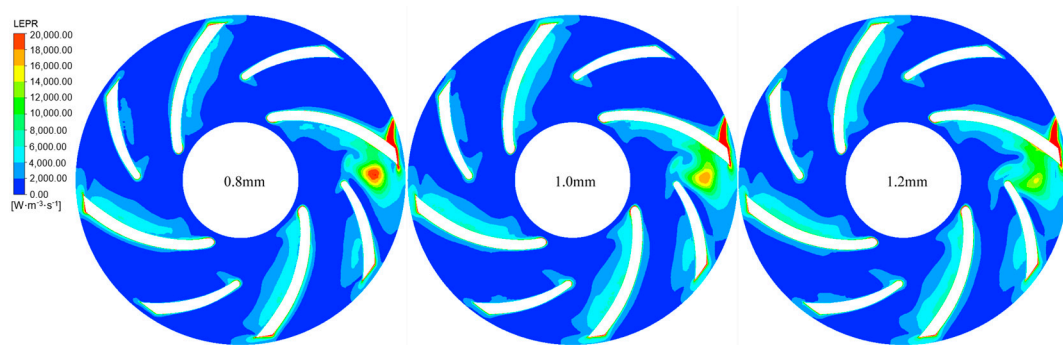


Figure 18. Distribution of local entropy yield of 90% height section of impeller blades.

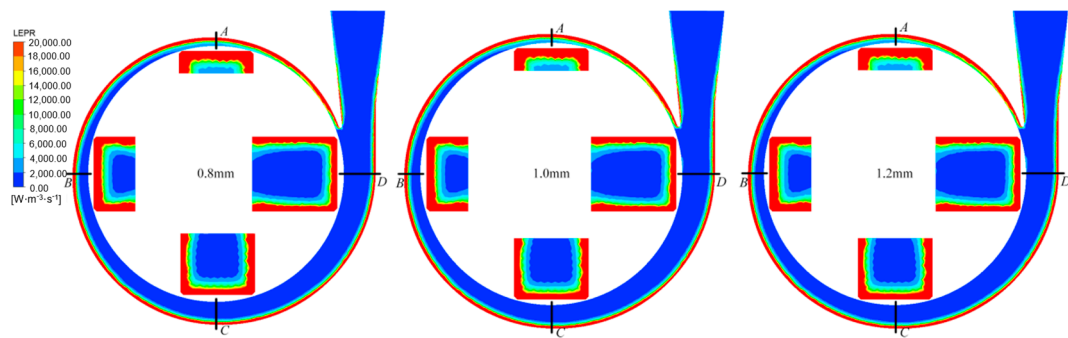


Figure 19. Distribution of local entropy production in the volute region.

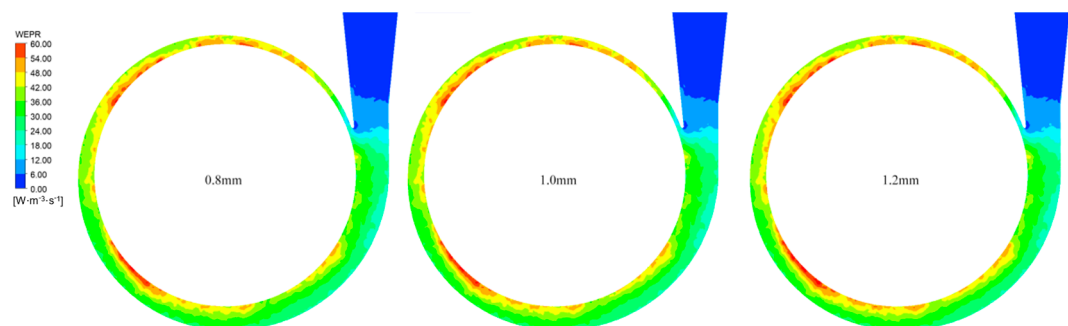


Figure 20. Distribution of entropy production rate on the wall of volute region.

5. Conclusions

The effect of crooked top clearance on the operation of high-speed centrifugal pumps is investigated in this article. Furthermore, an analysis of the pump's external properties, internal flow characteristics, and energy dissipation with respect to different lobe top clearance dimensions (0.8 mm, 1.0 mm, and 1.2 mm) is conducted using numerical simulation. The following conclusions can be drawn:

- (1) Increasing the flow rate results in a decrease in the head of high-speed centrifugal pumps, highlighting the optimal performance at 1.4 times the design flow rate ($1.4 Q_d$).
- (2) Numerical simulations of three high-speed centrifugal pumps with varying lobe top clearances were conducted under seven distinct flow conditions to generate external characteristic curves of head and efficiency. The simulations illustrated that the head diminishes in tandem with the increase in flow rate and lobe top clearance. This suggests that the flow of clearance leakage increases as the split top clearances increase, resulting in a decrease in pump head and increase in volume losses. At low flow rates, the efficiency of the split top clearance is minimally affected; however, at higher flow rates, a modest clearance considerably increases efficiency.
- (3) Changes in lobe clearance have a minimal impact on the pressure distribution within the impeller, but they substantially influence the velocity distribution, particularly near the suction surface, as demonstrated by the analysis of the flow field within the pump under design flow conditions. The flow becomes more intricate as a result of the increased backflow and energy losses at the tongue, as well as the formation of additional vortices near the suction surface of the impeller.
- (4) The investigation of energy dissipation revealed a modest increase in overall entropy production as the cleft clearance widened. This is consistent with the observed decrease in efficacy. Despite the fact that the volute experiences the most significant energy losses, the impeller and lobe clearance experience a marginal increase in energy loss as clearance values increase.

This investigation demonstrates the substantial impact of lobe top clearance on the performance of high-speed centrifugal pumps, including efficiency, head, flow, and other

critical parameters, through a systematic analysis of various lobe top clearances. We discovered that the pump's operating efficiency can be substantially enhanced while maintaining a stable fluid transfer capacity by optimizing the lobe top clearance. The engineering design and operation of the space station are significantly affected by the discovery. The pump's efficacy can be optimized by modifying the lobe top clearance to the optimal value, which is particularly critical given the space station's limited energy supply. Efficient pump designs have the potential to decrease energy consumption and maintenance frequency, which is particularly advantageous for space stations that operate in remote locations with limited resupply options. In summary, this investigation offers a critical reference for enhancing the reliability and performance of the fluid power apparatus of the space station by conducting a comprehensive examination of the impact of the crooked top clearance of the high-speed centrifugal pump on its performance. We are of the opinion that these discoveries will have a beneficial influence on the design and operation strategies of future space stations, thereby enabling humanity to make more substantial strides in the field of space exploration.

Author Contributions: D.W. (Dongxu Wang): methodology, software, writing—original draft. K.W.: formal analysis, writing—review and editing. Z.W.: data curation, visualization. D.W. (Dongwei Wu): writing—review and editing. Y.S.: validation, data curation, writing—review and editing. All authors have read and agreed to the published version of the manuscript.

Funding: This research received no external funding.

Data Availability Statement: The original contributions presented in the study are included in the article, further inquiries can be directed to the corresponding author.

Conflicts of Interest: Author Dongwei Wu was employed by the Jiangsu Surveying and Design Institute of Water Resources Co., Ltd. The remaining authors declare that the research was conducted in the absence of any commercial or financial relationships that could be construed as a potential conflict of interest.

References

1. Zheng, X.; Luo, W.; Hu, Y.; He, Z.; Wang, S. Analytical approach to mesh stiffness modeling of high-speed spur gears. *Int. J. Mech. Sci.* **2022**, *224*, 107318. [[CrossRef](#)]
2. Zhao, P.; Gao, X.; Su, Y.; Xu, Y.; Huang, Y. Investigation of seeding performance of a novel high-speed precision seed metering device based on numerical simulation and high-speed camera. *Comput. Electron. Agric.* **2024**, *217*, 108563. [[CrossRef](#)]
3. Zhu, Z.C.; Chen, Y.; Jin, Q.M.; Huang, D.H. Study on high-speed centrifugal-regenerative pump with an inducer. *Chin. J. Chem. Eng.* **2002**, *10*, 137–141.
4. Zhang, Z.; Guo, Q.; Ye, P.; Xu, Q.; Chen, Z.; Ji, Q.; Ke, C.; Meng, F. Preparation and performance of nanofibers by centrifugal spinning with multi-field coupling. *J. Text. Inst.* **2023**. [[CrossRef](#)]
5. Zhang, J.; Yang, H.; Liu, H.; Xu, L.; Lv, Y. Pressure Fluctuation Characteristics of High-Speed Centrifugal Pump with Enlarged Flow Design. *Processes* **2021**, *9*, 2261. [[CrossRef](#)]
6. Wu, Y.; Lu, P.; Lin, F.; Bao, W.; Qu, M.; Li, P.; He, H. Explosion accident analysis of ultra-high-speed grinding wheel. *Eng. Fail. Anal.* **2021**, *122*, 105209. [[CrossRef](#)]
7. Yan, S.; Ye, Z.; Wang, D.; Ma, J.; Zhou, W. Structural Analysis and Optimization of Ultra-High-Speed Centrifugal Pump Rotor System Considering Fluid-Structure Interaction. *Water* **2024**, *16*, 1471. [[CrossRef](#)]
8. Zhang, Q.; Yang, D.; Kong, Q.; Sun, X.; Hu, Z. A super-high-speed PM motor drive for centrifugal air compressor used in fuel cell unmanned aerial vehicle. *IET Electr. Power Appl.* **2023**, *17*, 1459–1468. [[CrossRef](#)]
9. Cong, X.; Xiao, J.; Li, H.; Yang, D. Multi-objective optimization design of water and dynamic performance of high-speed centrifugal pump. *Fluid Mach.* **2022**, *50*, 27–34.
10. Zhou, Z.; Wang, H.; Wang, G.; Li, X.; Lin, Q. Effect of mouth ring clearance on the performance of double-stage high-speed centrifugal pump. *Rocket Propuls.* **2023**, *49*, 66–72.
11. Wang, R. Study on the Optimal Design and Cavitation Characteristics of the High-Speed Induced Wheel Centrifugal Pump. Master's Dissertation, Jiangsu University, Zhenjiang, China, 2022.
12. Zhu, Q. Hydraulic Design and Numerical Simulation of Ultra-Low Specific Speed and High-Speed Centrifugal Pump. Master's Dissertation, Yangzhou University, Yangzhou, China, 2017.
13. Sha, Y. Study on 3 d Turbulence Numerical Simulation and Flow Characteristics of High Temperature and High Pressure Centrifugal Pump. Master's Dissertation, Tsinghua University, Beijing, China, 2011.

14. Zhao, L. Internal Flow Field Analysis of Centrifugal Pump at High Speed. Master's Dissertation, Xi'an University of Technology, Xi'an, China, 2014.
15. Zhou, L. Study on Hydraulic Optimization and Numerical Simulation of Ultra-High-Speed Centrifugal Pump. Master's Dissertation, Chang'an University, Xi'an, China, 2021.
16. Liu, C.; Qin, D.; Liao, Y. Dynamic modeling and analysis of high-speed planetary gear including centrifugal force. *J. Braz. Soc. Mech. Sci. Eng.* **2017**, *39*, 3769–3778. [[CrossRef](#)]
17. Lin, C.W.; Tu, J.F.; Kamman, J. An integrated thermo-mechanical-dynamic model to characterize motorized machine tool spindles during very high speed rotation. *Int. J. Mach. Tools Manuf.* **2003**, *43*, 1035–1050. [[CrossRef](#)]
18. Liang, H.; Guo, D.; Ma, L.; Luo, J. Experimental Investigation of Centrifugal Effects on Lubricant Replenishment in the Starved Regime at High Speeds. *Tribol. Lett.* **2015**, *59*, 3. [[CrossRef](#)]
19. Li, S.; Wang, Y.; Wu, Y.; Zhang, K.; Zhang, L. The processing and application of a zirconia ceramic shaft. *Mater. Res. Innov.* **2015**, *19*, S5-376–S5-379. [[CrossRef](#)]
20. Lai, T.; Yan, S.; Wang, Y.; Liu, X.; Qiang, M.; Ding, W.; Liu, Y.; Hou, Y. Numerical study on static performance of hydrodynamic bearing in high-speed liquid hydrogen centrifugal pump. *Int. J. Hydrogen Energy* **2023**, *48*, 1552–1567. [[CrossRef](#)]
21. Kong, X.; Tang, J.; Hu, Z.; Chen, S.; Wang, Q. A new approach for analyzing internal load and fatigue life of deep groove ball bearing in high-speed gearbox system. *J. Vib. Control.* **2023**, *29*, 4972–4986. [[CrossRef](#)]
22. Kolondzovski, Z.; Cvetkovski, G. Thermal Study of Retaining Sleeves for a High-Speed Permanent-Magnet Electrical Machine. *Prz. Elektrotechniczn.* **2008**, *84*, 177–180.
23. Kim, K.H.; Oh, B.S.; Nahm, S.; Cheong, H.W.; Han, Y.S. Evaluation of high-speed rotation properties of LiCl-KCl molten salt with MgO binder. *Int. J. Nanotechnol.* **2022**, *19*, 3. [[CrossRef](#)]
24. Jorgensen, B.R.; Shin, Y.C. Dynamics of spindle-bearing systems at high speeds including cutting load effects. *J. Manuf. Sci. Eng.* **1998**, *120*, 387–394. [[CrossRef](#)]
25. Jiang, B.; Qi, C.; Xia, D.; Cao, S.; Chen, B. Dynamics Characteristic of Cutter Wear in High Speed Milling Hardened Steel. *Adv. Sci. Lett.* **2011**, *4*, 3103–3107. [[CrossRef](#)]
26. Jang, S.-M.; Cho, H.-W.; Choi, S.-K. Design and analysis of a high-speed brushless DC motor for centrifugal compressor. *IEEE Trans. Magn.* **2007**, *43*, 2573–2575. [[CrossRef](#)]
27. Hou, P.; Ge, B.; Tao, D.; Pan, B.; Wang, Y. Rotor Strength Analysis of FeCo-Based Permanent Magnet High Speed Motor. *Machines* **2022**, *10*, 462. [[CrossRef](#)]
28. Hao, Y.; Hao, J.; Zuchao, Z.; Xianghui, S.; Wenqi, L.; Gruszczynski, M.; Qiangmin, D.; Panlong, G. Review of the Hydraulic and Structural Design of High-Speed Centrifugal Pumps. *Front. Energy Res.* **2022**, *10*, 899093. [[CrossRef](#)]
29. Fu, H.G.; Xiao, Q.; Xing, J. Manufacture of centrifugal cast high speed steel rolls for wire rod mills. *Ironmak. Steelmak.* **2004**, *31*, 389–392. [[CrossRef](#)]
30. Feng, P.F.; Yu, D.W.; Wu, Z.J.; Uhlmann, E. Jaw-chuck stiffness and its influence on dynamic clamping force during high-speed turning. *Int. J. Mach. Tools Manuf.* **2008**, *48*, 1268–1275. [[CrossRef](#)]
31. Fang, J.; Liu, X.; Han, B.; Wang, K. Analysis of Circulating Current Loss for High-Speed Permanent Magnet Motor. *IEEE Trans. Magn.* **2015**, *51*, 1–13. [[CrossRef](#)]
32. Duan, Y.; Zhang, Z.; Lu, B.; Chen, B.; Lai, Z. The movement and forces of spinning solution in the nozzle during high-speed centrifugal spinning. *J. Eng. Fiber Fabr.* **2019**, *14*, 1558925019828207. [[CrossRef](#)]
33. Cui, B.; Chen, Z.; Zhang, Y. Influence of blade trailing edge profile on pressure pulsation in high-speed centrifugal pump. *AIP Adv.* **2024**, *14*, 065107. [[CrossRef](#)]
34. Chen, J.-S.; Hwang, Y.-W. Centrifugal force induced dynamics of a motorized high-speed spindle. *Int. J. Adv. Manuf. Technol.* **2006**, *30*, 10–19. [[CrossRef](#)]
35. Chatterjee, S. Spindle deflections in high-speed machine tools—Modelling and simulation. *Int. J. Adv. Manuf. Technol.* **1996**, *11*, 232–239. [[CrossRef](#)]
36. Cao, H.; Holkup, T.; Chen, X.; He, Z. Study of characteristic variations of high-speed spindles induced by centrifugal expansion deformations. *J. Vibroeng.* **2012**, *14*, 1278–1291.
37. Bang, K.G.; Lee, D.G. Thrust bearing design for high-speed composite air spindles. *Compos. Struct.* **2002**, *57*, 149–160. [[CrossRef](#)]

Disclaimer/Publisher's Note: The statements, opinions and data contained in all publications are solely those of the individual author(s) and contributor(s) and not of MDPI and/or the editor(s). MDPI and/or the editor(s) disclaim responsibility for any injury to people or property resulting from any ideas, methods, instructions or products referred to in the content.